Research Square

Preprints are preliminary reports that have not undergone peer review.
They should not be considered conclusive, used to inform clinical practice,
or referenced by the media as validated information.

Growing Synthetic Nacre: Simultaneous Deposition and Assembly of Interlocking Bricks

Mohammad Mirkhalaf

mohammad.mirkhalaf@qut.edu.au

Queensland University of Technology https://orcid.org/0000-0002-0917-8978

Zizhen Ding

Queensland University of Technology

Reza Shakibanezhad

Queensland University of Technology

Travis Klein

Queensland University of Technology https://orcid.org/0000-0002-6669-7766

Article

Keywords:

Posted Date: April 10th, 2026

DOI: https://doi.org/10.21203/rs.3.rs-8422568/v1

License: This work is licensed under a Creative Commons Attribution 4.0 International License.
Read Full License

Additional Declarations:
Yes there is potential Competing Interest. M. Mirkhalaf, Z. Ding, and T. Klein are inventors on provisional patent No. 2025905858 filed by the Queensland University of Technology, which covers the work reported in this article.

Version of Record: A version of this preprint was published at Communications Materials on July 8th, 2026. See the published version at https://doi.org/10.1038/s43246-026-01268-w.

Growing Synthetic Nacre: Simultaneous Deposition and Assembly of Interlocking Bricks

Zizhen Ding[1,2], Reza Shakibanezhad[1,2], Travis Klein[1,2], and Mohammad Mirkhalaf [1,2,3]*

[1] School of Mechanical, Medical and Process Engineering, Queensland University of Technology (QUT), 4000 Brisbane, QLD, Australia.

[2] Centre for Biomedical Technologies, Queensland University of Technology (QUT), 4059 Brisbane, QLD, Australia

[3] Centre for Materials Science, Queensland University of Technology (QUT), 4000 Brisbane, QLD, Australia

*Corresponding author: mohammad.mirkhalaf@qut.edu.au

Achieving ceramics that combine stiffness, strength, and toughness in complex geometries remains a major challenge, limiting their use in applications such as bone implants. Bio-inspired architectures – composed of stiff, strong building blocks connected by deformable interfaces – offer a promising solution. However, their implementation is constrained by limited control over the arrangement and composition of blocks, especially in constructs with complex shapes at centimeter- to meter-scale. We present a light-based printing method that deposits and assembles interlocking ceramic bricks onto connecting micro-pins, inspired by nacre's growth mechanism. A custom alumina resin was developed and printed using a tabletop LCD 3D printer, sintered, and subsequently infiltrated with polycaprolactone, a tough and biocompatible polymer that forms the deformable interfaces. The resulting nacre-like constructs, with 76-78 wt% (50-52 vol%) ceramic, showed flexural stiffness of 2.27 ± 0.44 GPa, strength of 41.4 ± 1.33 MPa, and energy absorption of at least 6.35 ± 0.97 MJ/m^3. These values match the energy absorption of cortical bone, exceed the rule-of-mixtures value by fivefold, and surpass that of monolithic ceramic by over 4,000 times. Finally, a 5 cm-long nacre-like construct replicating the geometry of the human tibia was fabricated and tested in flexion, demonstrating scalability and potential for biomedical applications.

Introduction

Ceramics are widely valued for their stiffness, strength, lightness, scratch resistance, and chemical versatility, enabling applications across aerospace, electronics, and biomedicine. Also, technical ceramics such as alumina have an overall ecological footprint similar to wood-based materials [1]. Yet their inherent brittleness and the difficulty of shaping them into complex geometries without compromising mechanical properties have yet constrained their broader utility. Nature offers a blueprint for overcoming these limitations [2-4]. Materials such as seashells, tooth enamel, and stomatopod dactyl club achieve remarkable toughness through precise architectures composed of stiff mineral building blocks connected by energy-dissipative interfaces [5-7]. The stiffness and strength arise from the building blocks, while toughness is imparted by the interfaces and architecture. Interfaces impede crack propagation, and architecture enables progressive sliding of the blocks, resulting in deformability. These mechanisms lead to outstanding toughness amplification [8]. For example, nacre from seashells has a brick-wall architecture composed of 95 wt% brittle aragonite platelets, yet exhibits a toughness of 1–2 $kJ \cdot m^{-2}$ – nearly three orders of magnitude greater than that of pure aragonite [9].

Inspired by nacre, numerous nacre-like materials with exceptional mechanical properties have been developed over the past two to three decades. The fabrication techniques can be broadly classified into two main categories: (i) Bottom-up approaches, which begin with building blocks and assemble them into complex architectures, such as a nacre-like architecture. These methods include self-assembly [10-13], freeze casting [14-18], slip casting [19], 3D printing [20-25], and a variety of other methods, such as centrifugation and vibration, to mix and align particles [26-30]; and (ii) Top-down approaches, such as laser engraving [31-33], which start with bulk materials and sculpt internal architectures by carving interfaces within the material. Despite significant progress, practical application remains hindered by:

1. Precise control over building block shapes and arrangement (order), particularly in complex geometries,
2. Scalability of the order to centimeter- and meter-scale constructs, and
3. Limitations in tailoring the composition of building blocks. In biomedical contexts, the need for biocompatible materials further narrows the range of suitable constituents, imposing additional constraints on material selection.

Here, we report a fabrication procedure inspired by the natural growth of nacre by printing ceramic building blocks onto connecting micro-pins – similar to how aragonite platelets grow on mineral bridges in nacre (Fig. 1a-c) [4]. This method enables the simultaneous construction of both the building blocks and the architecture while leveraging the stiffening and strengthening roles of the micro-pins. The process provides full control over the shape, arrangement, and composition of the ceramic components, as well as the overall geometry of the construct. The shape of the building blocks can be tuned to achieve the desired mechanical properties in the anticipated loading condition, while the geometry can be tailored to fit the desired application.

Results

Fabrication

Overall Fabrication Process. We selected photopolymerization to grow ceramic building blocks on connecting micro-pins, a technique that offers the resolution needed to precisely define block geometry. Among available photopolymerization methods, liquid crystal display (LCD) 3D printing was chosen for its high resolution (tens of micrometers), scalability (up to tens of centimeters), cost-effectiveness, and industrial viability [34,35]. To enable simultaneous printing of building blocks, architecture, and overall shape, we developed a custom alumina ceramic resin (Fig. 1d). A nacre-like 3D architecture with geometrical interlocking between

platelets in adjacent layers was designed using SolidWorks (Dassault Systèmes, France) and printed using a commercial LCD printer with a printing resolution of 50×50×25 µm (Zortrax Inkspire 2, Olsztyn, Poland). The printer allowed selection of exposure intensity and duration for successful layer formation and was equipped with a resin mixer to prevent particle sedimentation. The printed ceramic green body was sintered to remove organic components, yielding a pure ceramic construct (Fig. 1b). This construct was subsequently infiltrated with biocompatible polymers, which served as the mortar phase between ceramic building blocks.

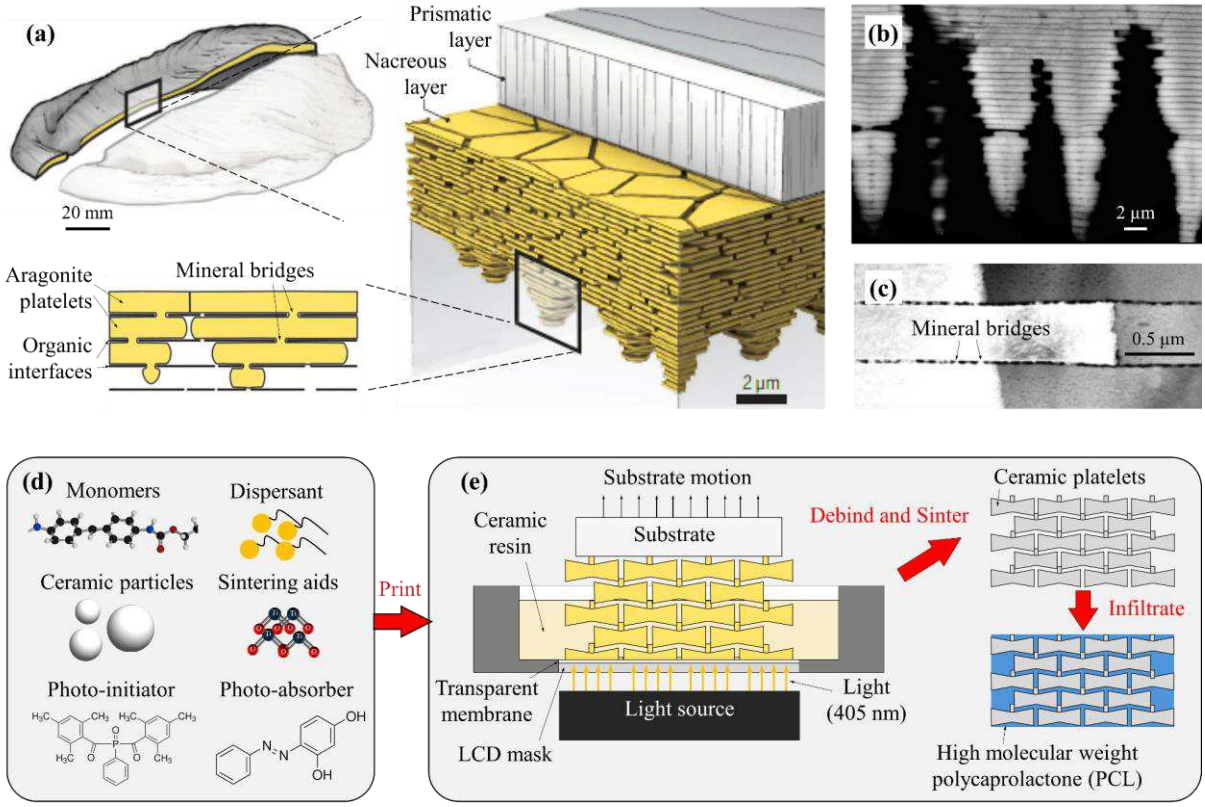


Fig. 1. Growing nacre-like materials. (a) The internal structure of a bivalve shell showing the growth of aragonite platelets on mineral bridges. Adapted from [36]. (b) and (c) SEM images showing the growth of platelets and the mineral bridges, respectively. Adapted from [37]. (d) The ingredients of the custom-made ceramic resin. (e) The fabrication process flow.

Custom Ceramic Resin Development. Ceramic resins have been developed previously, mostly to make porous ceramics, including our own work [38,39]. However, the use of commercial photopolymers in these resins limits fine-tuning of their viscosity, particle concentration, and

photoactivity to enable the combination of resolution and photo-reactivity needed to print building blocks on connecting micro-pins.

We formulated a ceramic resin with full control over particle size, distribution, and concentration, as well as photo-reactivity and viscosity. Successful light-based ceramic printing and sintering required meeting several interdependent conditions: (1) *High ceramic loading*: >50–70 wt% of fine ceramic particles with a mean particle size (D_{50}) typically less than 10 μm [40-42], (2) *Low resin viscosity*: ideally, less than 3000 mPa·s at a shear rate of 10 s^{-1} to ensure smooth flow and uniform layer spreading, (3) *Resin stability*: to prevent particle agglomeration over time, (4) *High photoactivity with fine resolution*: to ensure complete photopolymerization while maintaining feature fidelity. (5) *Low processing temperature*: below 60 °C to avoid degradation of photoactive components [43].

These parameters are interdependent; for example, increasing ceramic content raises viscosity [44], or increasing photo-initiator concentration enhances reactivity but may reduce resolution [45]. We addressed these requirements through the following strategies:

(1) *Selecting a monomer combination to ensure low viscosity and high bonding stability*. We selected 1,6-hexanediol diacrylate (HDDA) as the primary monomer due to its low viscosity [46]. Diurethane dimethacrylate (UDMA) was added as the secondary monomer to provide stronger and more durable polymer networks due to its four functional groups [47]. A 9:1 HDDA: UDMA ratio produced the lowest viscosity among the tested formulations (Supplementary Fig. 1).

(2) *Optimizing the photo-initiator to photo-absorber ratio to balance reactivity and resolution*. Sudan Orange G was added as a photo-absorber to improve printing resolution. An 8.5:1 ratio of photo-initiator to photo-absorber enabled successful printing with a minimum layer thickness of 25 μm.

(3) *Choosing a dispersant compatible with alumina to prevent agglomeration*. Solsperse AC5145 (Lubrizol, USA) was chosen for its compatibility with alumina and its ability to anchor onto hydroxyl groups on the particle surface, forming a stabilizing boundary. This prevented particle agglomeration and stabilized the ceramic resin [48-50].

(4) *Selecting a photo-initiator responsive to the LCD printer's wavelength (405 nm)*. Phenylbis (2,4,6-trimethylbenzoyl) phosphine oxide (BAPO) was selected as the photo-initiator due to its strong absorption at 405 nm, matching the emission spectrum of the LCD printer. This ensured efficient photopolymerization during printing.

(5) *Identifying the smallest achievable particle using wet ball milling to ensure stability in the resin during printing and facilitate sintering*. Wet ball milling was used to refine the alumina particle size, yielding a steady-state value of 3.11 ± 0.01 μm (Supplementary Fig. 2). This size remained stable during subsequent mixing, ensuring consistent dispersion and facilitating densification during sintering.

(6) *Adding the sintering aid to promote the sintering of alumina manufactured by 3D printing.* 0.5 wt.% of nano-sized Titanium Oxide (TiO_2) with respect to the weight of alumina powder was added to the resin formulation during the wet ball milling process to improve the flexural performance of the sintered alumina [51].

The final resin formulation contains 57 wt% refined alumina, was blended first with TiO_2, HDDA, UDMA, and Solsperse AC5145 via ball milling. Subsequently, BAPO and Sudan Orange G were added into the resin via a mechanical stirrer to prevent them from losing their vitality and enable effective photoinitiation and photoabsorption. This resulted in a resin exhibiting viscosity at ~1035 mPa·s at a low shear rate of 10 s^{-1} (MCR302 Rheometer, Anton Paar, Austria). The resin also exhibited shear-thinning behavior, favorable for ceramic 3D printing (Supplementary Fig. 1).

Printing Process. A minimum layer thickness of 25 μm was used for printing. Five combinations of laser light intensity in the range of 3 to 10 mW and exposure times in the range of 10 to 20s were explored, and the laser light intensity of 10 mW and an exposure time of 20s were used for printing. The detailed printing parameters are included in the Supplementary Information (Supplementary Fig. 3).

Ceramic Sintering Profile. Sintering relatively large ceramic parts with intricate internal structures and varying thicknesses presents two main challenges. The first is the friction between large surfaces (e.g., >10 cm × 1 cm) that undergo large shrinkage – around 50% – which can lead to cracking. To mitigate this, specimens were separated from the alumina crucible surface using a thin layer of alumina particles ($D_{50} \approx 100$ μm; Merck, USA). These particles, being large enough to avoid sintering or bonding with the printed parts, acted as mechanical rollers, effectively reducing stress buildup during shrinkage.

The second challenge arises from the varying thickness within the component, which can cause inhomogeneous shrinkage and cracking. To address this, a slow heating rate (1 °C/min) was used along with a multi-step sequence at 350 °C and 750 °C to burn off the organic component of the printed parts, followed by final two-step sintering at 1100 °C and 1650 °C in a muffle furnace (CF1800, Across International, Australia). These temperatures were selected based on thermogravimetric analysis (TGA) of the resin, while ensuring that the furnace's heating elements were not exposed to degrading conditions (Supplementary Figs. 4 and 5).

Polymer Infiltration and Interface Modification. Three polymers, Poly(methyl methacrylate) PMMA, Silicone, and High molecular weight polycaprolactone (PCL), all biocompatible polymers widely used in biomedical applications, were explored to form deformable interfaces between ceramic building blocks. PCL was ultimately selected and was vacuum infiltrated into the construct for its optimal combination of deformability, mechanical

strength, and adhesion to ceramic surfaces. To further improve the adhesion between PCL and the ceramic surfaces, a silanization procedure was conducted. (Detailed procedure and the comparison between different polymers can be found in the Methods section and Supplementary Fig. 6)

Design

To design the nacre-like architecture, we required a space-filling platelet tessellating into a mechanically interlocked structure in three dimensions. We began with a flat hexagonal unit, which can be seen as three rhombus prisms (Fig. 2a). To introduce interlocking between adjacent hexagonal blocks, while preserving its space-filling nature, the top and bottom faces of each rhombus prism were tilted inward by an angle θ. This transformation yielded a "three-dimensional bowtie" block geometry. To enable continuous ceramic printing and structural integration, a central connective pin was incorporated into each block. This pin serves as a mechanical anchor on which the subsequent layers can be deposited, analogous to mineral bridges in natural nacre, facilitating both alignment and load transfer across layers.

A cross-section of a single block and a 3D assembly are shown in Fig. 2a and b, respectively. The 3D bowtie shape is described by two geometrical parameters: (1) the aspect ratio $\rho = L/t$, the ratio of the platelet length L to its average thickness t, (2) the interlocking angle θ. The central thickness of the block must remain positive. This constraint leads to the following geometric condition (equation (1)):

$$\theta \leq \tan^{-1}\left(\frac{2}{\rho}\right) \tag{1}$$

The spatial arrangement of hexagonal platelets between adjacent layers is illustrated in Fig. 2b. The platelets are shifted in the neighboring layers to allow an overlap covering half of the platelet length. As such, each pair of hexagons in the upper layer is aligned with the center

points of micro-pins in the lower layer. The blocks in each layer are positioned with a lateral spacing g_l/t and stacked vertically with an interlayer spacing g_v/t, ensuring consistent alignment and interlocking across layers.

Equation (1) defines the boundaries of an admissible domain in the design space characterized by the aspect ratio ρ and the interlocking angle θ. Within this domain, these parameters can be tuned to generate a wide variety of geometries, as illustrated in Fig. 2c. To demonstrate the versatility of our fabrication technique in tuning the architecture, samples were printed using platelets with aspect ratios of 5 and 10 with an average thickness of 1.6 mm, and interlocking angles were varied within the geometrically admissible range. For the aspect ratio of 5, the interlocking angles of 5°, 10°, 15°, and 20° were implemented. For the aspect ratio of 10, the interlocking angles of 5° and 10° were used (see Fig. 2c). Throughout this exploration, the pin diameter, lateral spacing, and vertical spacing were kept constant. A circular fillet with a diameter of 0.3 mm was also incorporated at the base of the pin to remove the sharpness and, in turn, reduce the severity of the stresses in load transfer between the platelets. All architecture consisted of five layers of hexagonal platelets stacked vertically and connected via micro-pins. An example of a 3D-printed, sintered, and infiltrated sample is shown in Fig. 2d. The side view of the sintered sample, along with its corresponding SEM image, which illustrates the fillet formation around the base and the dense microstructure of the sintered ceramic, is shown in Fig. 2e. The minimum feature size between the platelets of ~70 μm and the minimum platelet thickness of ~ 600 μm have been achieved here.

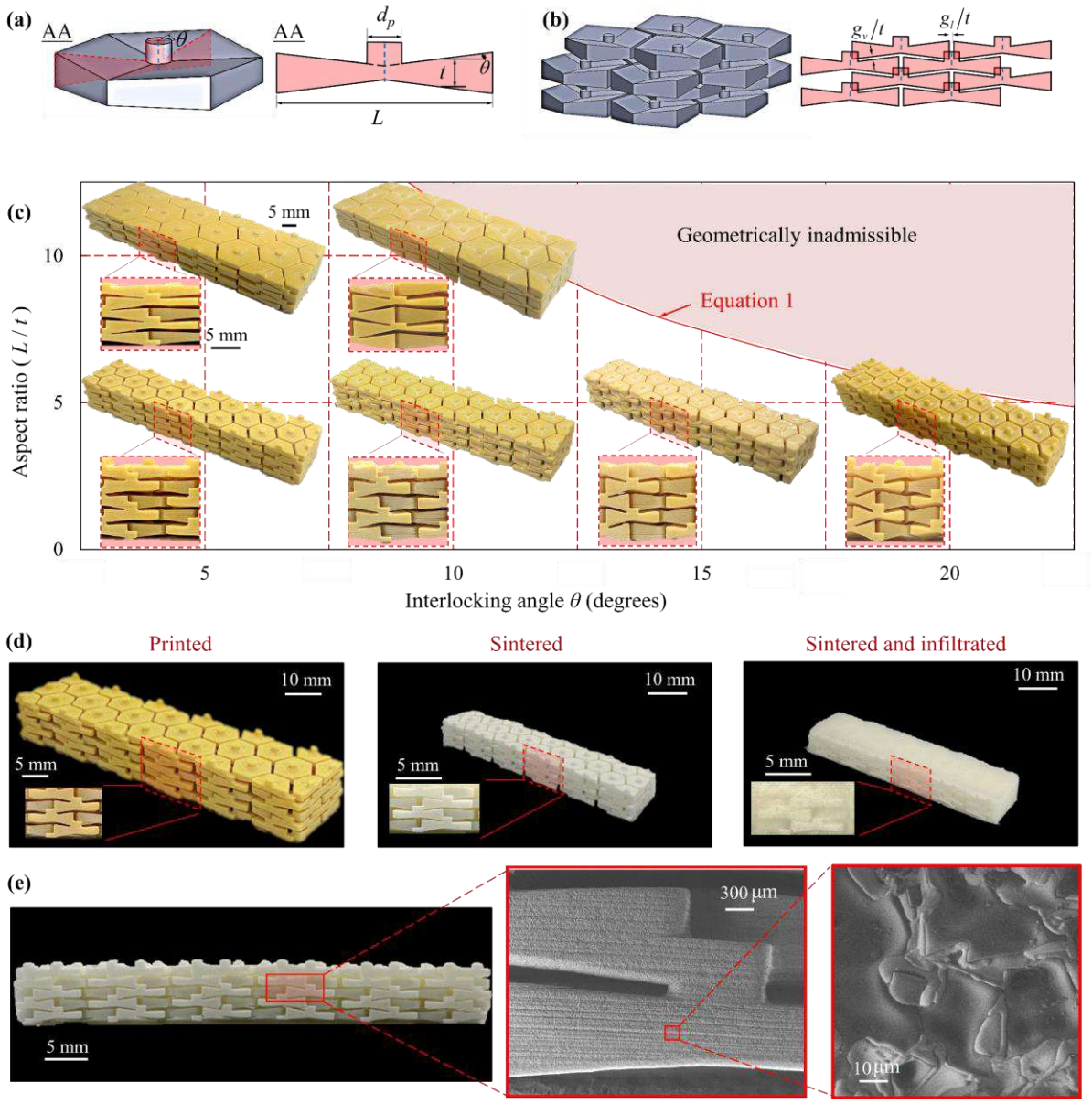


Fig. 2. The overall design of the nacre-like architecture. (a) The schematic of the design parameters of a single platelet. (b) The schematic of the spatial orientation between the platelets within the same layer and adjacent layers. (c) The range of geometries admissible for printing with different interlocking angles and aspect ratios. (d) The demonstration of the fully printed, sintered, and infiltrated sample that would be ready for the mechanical testing. (e) The side view of the sintered nacre-like architecture with the SEM images from different resolutions.

Mechanical performance

To evaluate the mechanical performance of the composites in flexion, we conducted a systematic study using samples with (1) a fixed aspect ratio $\rho = 5$ and various interlocking angles $\theta = 5^{\circ}$, 10°, 15° and 20°, and (2) a fixed interlocking angle $\theta = 10^{\circ}$ for various aspect

ratios ρ = 2.5, 5, and 10. The bending test was preferred over compression tests to specifically assess the material's resistance to crack initiation and propagation. Four-point bending was further preferred over three-point bending to apply a uniform bending moment across a larger volume of material, enabling: (1) enhanced defect sensitivity, as a larger volume better represents the bulk material and reveals the influence of internal flaws, if any, and (2) demonstration of strain delocalization, showcasing the material's ability to distribute deformation and absorb energy over a wide region. Displacement was measured using crosshead movement and corrected via manual image correlation, using the *in situ* optical images taken during the tests. Force data was obtained using a calibrated 2 kN load cell. Flexural stresses and strains were calculated assuming an equivalent homogeneous linear elastic material. The mechanical testing set-up can be found in Supplementary Fig. 7, and the calculations of stress and strain can be found in Supplementary Information.

Besides the flexural strain, we used optical images to quantify the deformation within the material using two complementary approaches: (1) displacement between platelets was measured to assess how deformation spread at different stages, and (2) the radius of curvature variation along the top edge of the specimen was analyzed to evaluate the uniformity or localization of deformation. The radius of curvature was measured at six equally spaced locations along the specimen's edge. Using MATLAB, edge points were detected, and arcs of circles were fitted to these points at each location and deformation stage. This allowed us to track changes in the radius of curvature ($1/r$) along the edge and over the course of deformation. An example flexural stress-strain behavior of the sample with ρ = 5 and $\theta = 5^{\circ}$ along with the in situ images, analysis of the deformation between the building blocks and radius of curvature variation along the edge are shown in Fig. 3. Supplementary Fig. 8 shows details of how we measure the radius of curvature at each position along the edge.

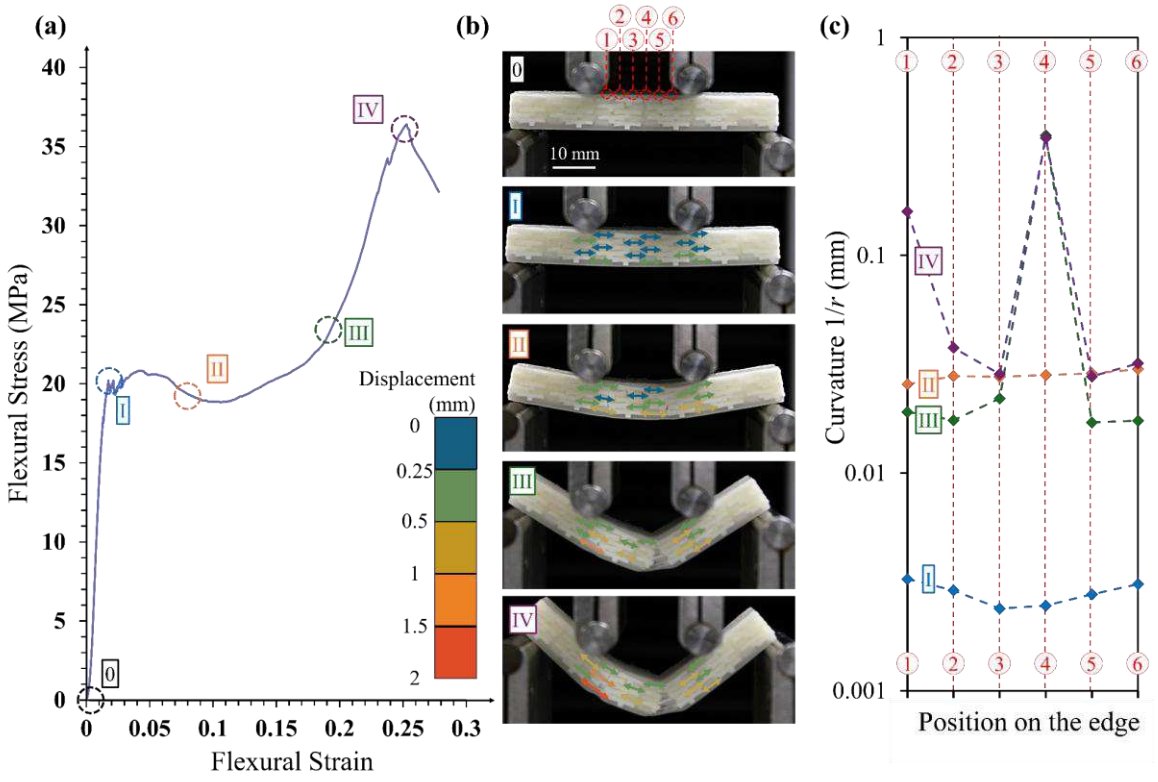


Fig. 3. **The stress-strain curve of representative bending test with its deformation analysis.** (a) The stress-strain curve of an infiltrated ceramic sample with an aspect ratio ρ = 5 and interlocking angle θ = 5°. (b) The displacement map between the platelets. The arrows represent the displacement between the platelets at different stages of deformation. (c) How the radius of curvature changes along the edge of the samples at different stages of deformation.

The deformation behavior of the material showed four distinct stages:

Stage 0-I (Elastic Region): The elastic regime extended to ~1.2% strain. At point I, audible cracking was detected, which we attributed to the failure of micro-pins between platelets. No cracks were observed at the platelets. The radius of curvature at the edge remained uniform across six locations. The displacement between the building blocks in the gauge area was ~ 0.25 mm at the outermost layer of the specimen and decreased towards the inner parts. No decrease in the distance between the blocks was observed in the compressive side, which we attributed to the stiffening role of connecting micro-pins.

Stage I-II (Yielding and Sliding): The stress-strain behavior plateaued, and the materials showed large deformations. Despite being 52 vol% ceramic, the composites exhibited ductile-like behavior, with no visible cracks at the platelets and no delamination between the ceramic

and polymer up to ~ 10 % flexural strain. The radius of curvature at the edge increased by seven times but remained yet uniform with no sign of localization in the radius of curvature or in the deformation maps. The displacements between the building blocks increase to 0.5-1 mm at the outer layer, and to 0-0.5 mm range at the inner layer.

Stage II-III (Crack Propagation and Ligament Formation): Initial cracks occurred in the outermost ceramic platelets at approximately 10–20% strain. As a result, stress was redistributed to the adjacent inner layers. The displacements between the building blocks kept increasing to the 0.5-1.5 mm range at the outermost ceramic layers, while those in the inner layers all increased to 0.25-0.5 mm. Deformation started to localize around the initially fractured platelets, leading to the subsequent failure of neighboring platelets in the second layer, particularly those near the original fracture sites. This localized deformation was also seen in the changes of the radius of curvature, where the values started to localize around the fourth position (Point "4") on the curve (the failure point of the sample) (Fig. 3b). Despite this localization of deformation, overall stress did not drop significantly, likely due to:

1. Incomplete crack penetration across the specimen width; each crack was confined within a single platelet.
2. Formation of PCL ligaments that (i) bridged the crack and (ii) pulled on the fractured interlocked pieces to further interlock and resist load. These ligaments played a significant role in preventing a drop in force. Tensile tests on PCL showed a hardening behavior up to around 350% strain (Supplementary Fig. 9).

Stage IV (stress started to decrease): As cracks propagated through most layers, stress began to decline at around 25% strain, exceeding typical strain thresholds observed in materials with similar 50-60 vol% ceramic content [52-54]. The radius of curvature continued to localize at the failure points of the sample: the fourth position (point "4"), where cracks appeared before, and

the first position (point "1"), where new cracks started to appear in the outermost layer at this stage.

Overall, this deformation behavior, consistent across most interlocking angles and aspect ratios, revealed four distinct toughening mechanisms: (1) interlayer platelet sliding demonstrated by increased distance between the platelets at the initial stages of deformation at the absence of cracks, (2) distributed deformation across the structure, (3) ligament formation by the polymer phase that showed hardening under tensile load, and (4) stress relocation and redistribution.

The effect of the interlocking angle. The flexural stress-strain and force-displacement curves of samples with $\rho = 5$ and $\theta = 5^{\circ}$, 10°, 15°, and 20° are shown in Fig. 4a and Supplementary Fig. 10, respectively. Interlocking angles above 20° were geometrically inadmissible (equation (1)). Overall, all samples exhibited similar overall stress–strain behavior across different interlocking angles (Fig. 4a). Each material showed an initial linear elastic response followed by plastic deformation with hardening, before stress began to decrease at around 20-25% strain. A summary of the four-point bending tests is presented in Fig. 4b. The results show that increasing the interlocking angle from 5° to 20° slightly enhanced the modulus by 1.1 times, flexural strength, and total energy absorption by 1.2 times. The effect of interlocking angles on modulus was more significant than on strength and energy absorption. As the interlocking angle increased, sliding became more constrained, and the modulus increased. However, similar mechanisms of platelet failure, ligament formation, and stress relocation governed the failure of the specimens, so the values of strength and energy absorption showed less improvement with increasing the interlocking angle. This behavior is consistent with observations in other architected materials, such as 3D-printed angled layers under tensile loading [55].

To ensure repeatability of the results, we repeated the tests for $\rho = 5$ and $\theta = 20^{\circ}$. We did not repeat the test for all configurations as we did not observe a significant variation by altering the interlocking angle, while the highest angle $\theta = 20^{\circ}$ showed slightly higher performance. The stress-strain curves for these repetitions are shown in Supplementary Fig. 11. The modulus, flexural strength, and energy absorption (at 25% strain) of the material are, respectively, 2.27 $\pm$ 0.44 GPa, 41.4 $\pm$ 1.33 MPa, and 6.35 $\pm$ 0.97 MJ/m^3, matching values reported for cortical bone [56]. The failure was graceful, not catastrophic. However, we could not do tests for strains larger than ~ 30% because the specimens started to touch the loading stage. The actual energy absorption of the nacre-like composites up to the failure, therefore, is more than the values reported here.

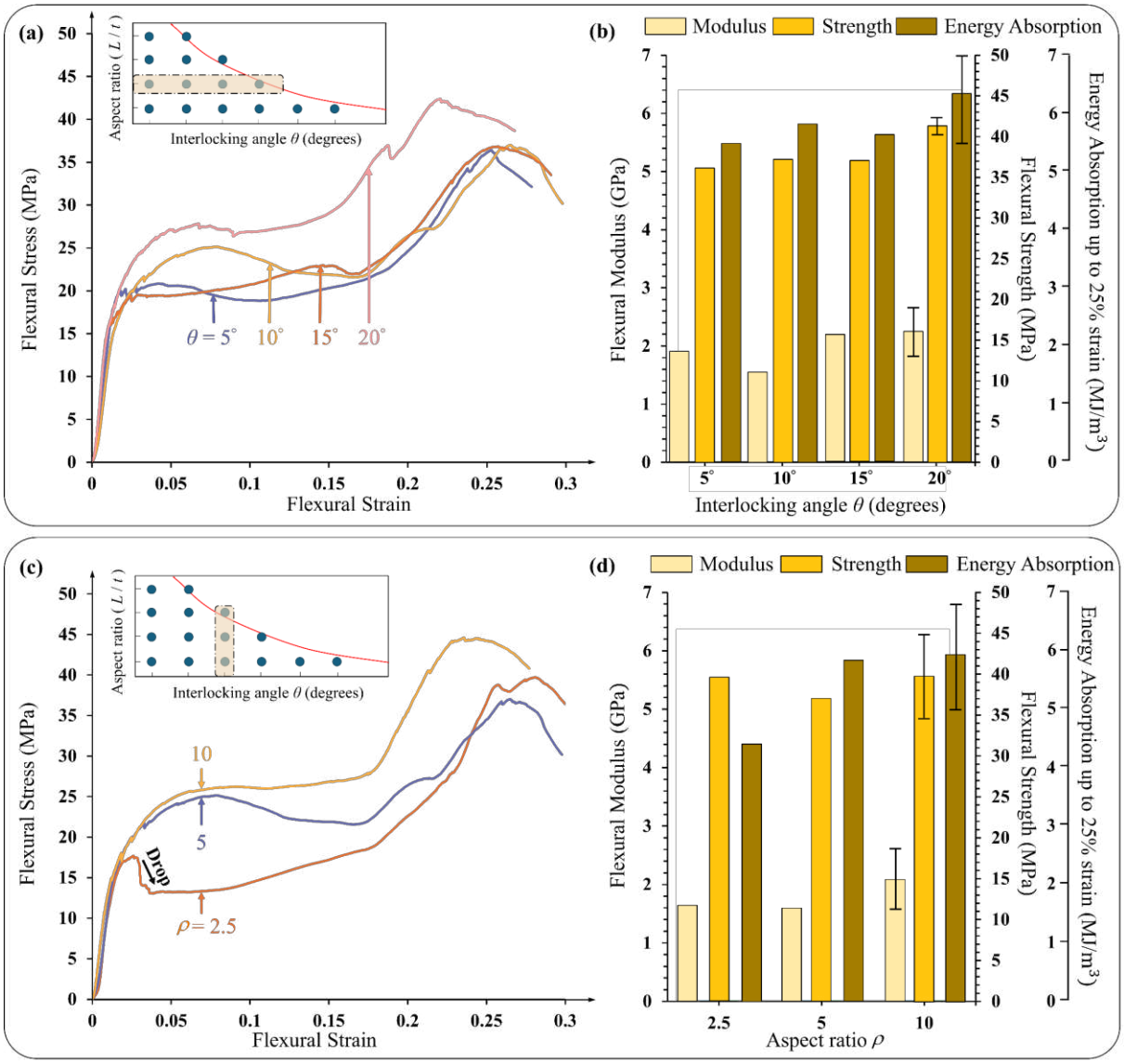


Fig. 4. The mechanical properties of nacre-like composites with different interlocking angles and aspect ratios. (a) The stress-strain curve of the composite with different interlocking angles. (b) The summary of the strength, modulus, and total energy absorption of the composite with different interlocking angles. (c) The stress-strain curve of the composite with different aspect ratios. Their corresponding mechanical properties are summarized in (d).

The effect of aspect ratio. To examine the effect of aspect ratio, samples with $\rho = 2.5$, 5, and 10 were tested, all having the same interlocking angle $\theta = 10^\circ$. Higher aspect ratios were not geometrically admissible for $\theta = 10^\circ$ (equation (1)). The resulting stress–strain curves are shown in Fig. 4c. The overall deformation and failure for all aspect ratios followed the same stages I to IV, as discussed for $\rho = 5$ and captured in the corresponding *in situ* optical images (Supplementary Fig. 12). The results show that increasing the aspect ratio did not significantly

change the elastic modulus or flexural strength. However, the energy absorption of the samples increased with increasing aspect ratios from 2.5 to 5 by around 33%.

At $\rho = 5$, the failure was entirely governed by the platelet failure (Fig. 3), and no platelet pull-out was observed. Decreasing the aspect ratio to 2.5 resulted in a mix-mode failure where some of the platelets, particularly at the outer tensile side of the specimens, pulled out (Supplementary Fig. 13), resulting in a significant drop in the force at the onset of stage I-II of the deformation, shown in Fig. 4c. This force drop resulted in a reduction in the overall area under the curve at small aspect ratios $\rho = 2.5$, compared with higher aspect ratios $\rho = 5$, and 10. However, the ultimate strength of the material was not affected by the aspect ratio, as the tablet pull-out was predominantly observed at the outermost layer of platelets, and the final failure was yet governed by the platelet fracture at the inner layers (Supplementary Fig. 13).

The results showed that for these nacre-like materials, increasing ρ and θ to the highest geometrically admissible combinations – governed by equation (1) – results in improved performance. At these high aspect ratios and interlocking angles, the platelets reached their load-bearing capacity, and the platelet failure was the dominant mode of failure. The individual platelet failures, however, did not result in a reduction in load as the PCL ligaments, formed post platelet fracture, showed significant hardening. The overall force started to significantly decrease only when most platelets fractured or pulled out, with pull-out only observed at small aspect ratios.

To confirm the repeatability of the results, we repeated the four-point bending test on three samples with $\rho = 10$ and $\theta = 10^\circ$ (Supplementary Fig. 11). Like the study of the effects of interlocking angle, we did not do the repetitions for smaller aspect ratios, as altering the aspect ratio did not significantly change the overall deformation behavior. For $\rho = 10$ and $\theta = 10^\circ$,

we found the flexural modulus of 2.11 ± 0.53 GPa, flexural strength of 39.50 ± 5.5 MPa, and total energy absorption of $5.95 \pm 0.96\,\mathrm{MJ/m^3}$.

Table 1 compares the modulus, maximum strength, and energy absorption of the composite (up to 25% strain) with those of pure alumina, PCL, as well as the values of the rule of mixture – upper bound for the modulus of the composite [57]. The stress-strain of PCL and ceramic are provided in Supplementary Information (Supplementary Fig. 14). As we couldn't break the PCL block using 4-point bending, and to capture the strength of the used PCL, we have used tensile tests on PCL dog-bone samples for comparison. The results indicate that the energy absorption of the nacre-like composite is five times higher than the value predicted by the rule of mixture, demonstrating the effectiveness of the nacre-like architecture and the discussed toughening mechanisms in yielding composites that outperform their constituents in terms of energy absorption and toughness. The elastic modulus and strength of nacre-like composites were, however, and as expected, respectively, thirty times and three times lower than the value of the rule of mixture.

These comparisons can be more accurate considering the actual energy absorption of alumina. In the composite and the polymer, energy dissipation occurs through the plastic deformation of the polymer, leading to a progressive failure; thus, the area under the curve truly represents the energy absorption of the material. However, for brittle materials like alumina, the area under the curve does not represent the true energy dissipation, as the failure is catastrophic and much of the energy is dissipated through dynamic effects and transferred to the test fixtures [58]. In all the ceramic samples tested under bending, a single crack consistently formed at the middle of the beams, creating a flat surface. This resulted in the area formed by the crack being the cross-sectional area of the beams ($\approx 2.1\times10^{-6}\ \mathrm{m^2}$). Thus, by multiplying the critical energy release rate $G_c = 27\ \mathrm{J/m^2}$ for alumina [59] to the cross-sectional area, we could determine the

actual energy absorbed to be $\sim 5.7\times10^{-5}$ J. The volume of the loaded material between the spans of the four-point bending tests was 3.9×10^{-8} m^3, and thus the actual energy dissipation of the ceramic per unit volume was $0.00145\,MJ/m^3$. Considering this value, the energy absorption of the nacre-like composite is more than 4,000 times higher than that of the ceramic and more than five times higher than the rule of mixture.

Table 1 The summary of the mechanical properties of the composite and its main components, and the comparison to the rule of mixture. The value inside the bracket represents the actual energy absorption of the pure alumina ceramic.

	Modulus (GPa)	Strength (MPa)	Energy Absorption up to 25 % strain (MJ/m^3)
Pure ceramic	215 ± 12	210 ± 18	0.13 ± 0.017 (0.00145)
PCL	0.174	35.48	2.46
Composite	2.27 ± 0.44	41.4 ± 1.33	6.35 ± 0.97
Rule of mixture	111	126	1.25 (1.2)

Constructs with anatomical shapes

Our process of simultaneously growing the building blocks and shaping the internal architecture and external shapes enabled us to fabricate the nacre-like material in complex anatomical shapes. For example, a 50 mm long construct replicating the geometry of the human tibia was produced (Fig. 5a). The design process started with a three-layer nacre-like sheet sample with building blocks that have an interlocking angle $\theta = 5^{\circ}$ and aspect ratio $\rho = 5$. This sheet sample was then rolled into a column and deformed into the shape of a human tibia with three layers of interlocking building blocks, as shown in Supplementary Fig. 15. In bending, three layers would be on the tensile side and three on the compression side. The same design process was repeatable with a higher number of layers (Supplementary Fig. 16). The same

ceramic resin, sintering profile, silanization, and infiltration protocols were used for the fabrication. The outcome of each step of the fabrication is shown in Fig. 5a. The only difference to the beams was that, since we had a hole in the center of the construct, a silicone shaft was made and inserted into it before infiltration to prevent PCL from filling the center, thereby duplicating the shape of the marrow cavity in the tibia. Three-point bending was used to characterize the mechanical performance of this nacre-like tibia sample. The stress-strain curve is shown in Fig. 5b. The results show that the anatomical shape nacre-like construct showed similar bending behavior as the beam samples with 0.48 GPa in flexural modulus, 44.54 MPa in flexural strength, and 6.18 MJ/m^3 in energy absorption up to 25 % strain. Compared to beams, however, the stress started to decrease at larger strains around 80 % to 100 %, which we attributed to the size effects [60].

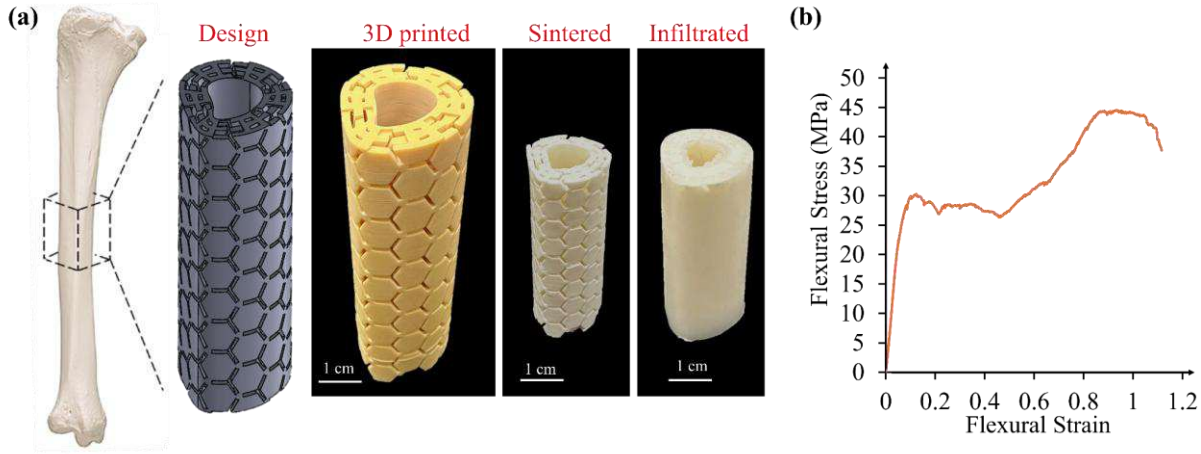


Fig. 5. Fabrication and mechanics of anatomically shaped constructs. (a) The designed, printed, sintered, and infiltrated construct replicating the shape of the tibia with 3 layers of platelets. (b) The stress-strain curve under the three-point bending test.

Discussion

Bioinspired materials composed of stiff, strong building blocks interacting through deformable interfaces offer a promising pathway toward achieving the long-sought combination of stiffness, strength, and toughness – a major challenge in materials science and engineering. Significant progress has been made in developing and understanding these systems,

particularly nacre-like brick-and-mortar composites. However, practical implementation remains limited by challenges in controlling the composition, shape, and arrangement of building blocks, especially in complex geometries and at scales relevant to real-world applications (centimeter to meter range).

In this work, a light-based fabrication technology was developed to simultaneously deposit and assemble alumina platelets on connecting micropins, resulting in a nacre-like architecture. The areas between these alumina platelets were then infiltrated by polycaprolactone (PCL). This approach enables precise control over the geometry and spatial arrangement of platelets, allowing the creation of complex shapes in sizes ranging from centimeters to tens of centimeters with a minimum feature size of ~70 μm (the distance between the platelets). The ceramic resin composition and choice of the infiltrating tough phase can be relatively easily tailored to change the composition of the final composites.

Example applications are anatomical shapes needed for the repair of critical-sized bone defects, which is yet an unmet clinical need. The resulting composites exhibit a flexural stiffness of 2.27 ± 0.44 GPa, a flexural strength of 41.4 ± 1.33 MPa, and energy absorption of 6.35 ± 0.97 MJ/m^3, matching the energy absorption of cortical bone, 4,000 times higher than the ceramic constituent, and more than five times higher than the rule of mixture. The stiffness and strength were respectively thirty times and three times lower than the values of the rule of mixture. The enhancement in energy absorption is attributed to the four distinct toughening mechanisms of platelet sliding, distributed deformation, ligament formation, and stress relocation and redistribution. These materials were also successfully formed into anatomically complex shapes representing segmental defects in the tibia, demonstrating the potential of this technology for load-bearing biomedical applications. Our approach bridges the gap between natural inspiration and scalable engineering, opening new avenues for the use of ceramics in biomedical and structural applications.

Outlook. The mechanical performance of our constructs is currently limited by the stiffness and strength of the base ceramic. These properties can be enhanced by increasing the particle loading in the resin and incorporating a combination of nano- and micro-scale ceramic particles – approaches that have been used before to improve the properties of ceramics [61] but not yet implemented in 3D printed ceramics, particularly the ceramic made of space-filling building blocks reported here. While these approaches increase resin viscosity, it can be mitigated by heating the resin bath to a temperature below the degradation threshold of the photoinitiator and photoabsorber, thereby reducing viscosity to an acceptable range.

The optimization of the architecture is material-dependent, and for each set of ingredients and interface conditions, various architectural effects can be discovered. Platelet failure was not a detrimental mode of failure in the nacre-like materials made of alumina and PCL reported here, due to a significant PCL ligament formation post failure of platelets and the hardening behavior of PCL in tension. However, it can be a detrimental mode of failure if other materials are used. Also, we did not observe delamination between the two phases due to the silanisation of surfaces. Studying the effects of materials and their interface behavior on architecture-performance relationships and optimum architecture deserves further theoretical and experimental studies.

Similarly, size can play a significant role in the mechanics of the materials. In this study, our samples consisted of five layers of interlocking blocks. Tests on samples with fewer layers (e.g., three) showed reduced flexural strength, primarily due to more pronounced edge effects (Supplementary Fig. 17) [60]. These effects diminish as the number of layers increases. Exploring these size effects, considering the size limitations imposed by the applications, and the resolution limitations imposed by the manufacturing techniques, deserve further investigation.

Improving the resolution of the printing process, through, for example, the use of more precise light sources and diverse pathways for photopolymerization inhibition, could help mitigate size effects and further enhance mechanical performance. For example, two-photon polymerization of polymer-derived nanoscale ceramic platelets holds promise for creating bio-inspired composites that leverage the exceptional strength of nanoscale ceramics while retaining the deformability and toughness imparted by the architecture and the printing paradigm implemented here. Moreover, additional biocompatibility, in vitro, and in vivo studies are necessary to prove the clinical applicability of the constructs developed here.

Methods

Preparing the ceramic powder

We used a commercially available alumina powder (Sigma Aldrich product code 11028) as an example material to demonstrate the 3D printing process. Colloidal ball milling was used to refine the particles from $D_{50} = 97$ μm to $D_{50} = 3.11 \pm 0.01$ μm inside a zirconia ball milling jar. The procedure started with mixing 28 wt% of the particles with 50 wt% zirconia balls and 22 wt% ethanol. The zirconia balls had four different diameters: 20, 15, 3, and 1 mm, with weight ratios of 27 %, 18%, 25%, and 25 %, respectively. The mixture was ball milled for 180 min at 250 rpm (pulverisette 5, FRITSCH, Germany). This speed was chosen as it is the maximum rotational speed allowed by the milling machine. The refined slurry was then dried at 150 °C for 24 hours. The dried powder was manually ground using a mortar and pestle and was filtered through a 315 μm sieve to remove the large clusters. The size of the refined ceramic particles was characterized using a laser diffraction analysis (Mastersizer 3000, Malvern Instruments, UK). The particle size reached a semi-steady state value with $D_{50} = 3.11 \pm 0.01$ μm after 180 mins refinement – the particle size that we used in this work (Supplementary Fig. 2).

Printing samples

In this study, the ceramic resin was prepared with 57 wt% refined alumina ceramic powder with $D_{50} = 3.11 \pm 0.01\,\mu m$ as the solid phase content. This particle concentration was chosen to maintain a suitable viscosity (< 3000 mPa·s), which ensured proper resin flow during the printing process and gave the sample a high density ($3.82\ g/cm^3$) after sintering. 0.5 wt% of Titanium Oxide nanoparticles (Sigma Aldrich product code 1003746316, US) with respect to the weight of alumina powder was used as the sintering aid to promote the sintering to have a defect-free ceramic lattice structure. 1,6-Hexanediol diacrylate (HDDA, Sigma Aldrich) and Diurethane dimethacrylate (UDMA, Sigma Aldrich) were mixed at a 9:1 ratio and magnetically stirred at 200 rpm for 30 minutes to be used as resin monomers. Solsperse AC5145 (Lubrizol, USA), phenylbis (2,4,6-trimethylbenzoyl) phosphine oxide (BAPO, Sigma Aldrich), and Sudan Orange G (Sigma Aldrich) were employed as the dispersant, photoinitiator, and photoabsorber. The ratio between monomers and dispersant was 3.4 to 1. The ratios of the BAPO and Sudan Orange G were respectively 0.3 wt% and 0.0353 wt% with respect to the monomers. All components were mixed by ball milling at 200 rpm for three hours with a ball: material ratio of ~ 1:1 to ensure homogeneous mixing. The stock resins were kept in glass containers wrapped with aluminum foil to prevent exposure to light.

The Zortrax Inkspire 2 printer (Olsztyn, Poland) was then used to print the specimens. The maximum laser light intensity of $10\ mW/cm^2$ and exposure time of 20s that are supported by the printer were applied to our resin. To achieve a fine resolution of printing, a minimum layer thickness of $25\,\mu m$ was used. The printing process used a clean resin bath with a wiper to mix and recoat the resin in the resin bath. The wiper frequency was set after every 5 layers and at 30 mm/s to ensure uniform and homogeneous recoating of the resin. The detailed printing settings can be found in Supplementary Fig. 3.

Sintering samples

After printing, the ceramic green bodies were sent to a high-temperature furnace (CF1800, Across International, Australia) for sintering and debinding. The thermogravimetric analysis (TGA) of the resin between 30 °C and 1600 °C at a heating rate of 20 °C/min revealed four distinctive decomposition peaks at 156.9 °C, 285 °C, 407.5 °C, and 534.6 °C (Supplementary Fig. 5). The manufacturer recommended against operating the CF1800 muffle furnace for a long time below 250 °C and between 400 °C and 700 °C to protect the furnace's heating elements. Thus, we have set a multi-step heating sequence of 350 °C and 750 °C for 6 hours to cover the decomposition peaks and burn off the organic component of the printed parts without compromising the heating elements. To address the inhomogeneous shrinkage and cracking caused by the varying thicknesses within the printed component, a slow heating rate (1 °C/min) was used for debinding. This was followed by sintering at 1100 °C to allow the titanium oxide nanoparticles to diffuse, and at 1650 °C for 6 hours in a muffle furnace to allow the samples to be fully dense and sintered. A median heating rate of 2 °C/min was used for the sintering phase to allow the sample to uniformly densify. (See Supplementary Fig. 4 for the detailed sintering profile).

To mitigate cracking of the specimens during the sintering process due to friction with the crucible and significant shrinkage (around 50 %), specimens were separated from the alumina crucible surface using a thin layer of alumina particles ($D_{50} \approx 100$ µm; Merck, USA). These particles, being large enough to avoid sintering or bonding with the printed parts, acted as mechanical rollers, effectively reducing stress buildup during shrinkage.

The silanization protocol

All ceramic constructs were surface silanised with 3-aminopropyltriethoxysilane (APTES, Sigma Aldrich Product Code:1003777183). Before the silanization process, the sintered

ceramic pieces were placed in pure ethanol and ultrasonicated for 1 minute to clean and introduce some hydrogen molecules on the surface. The pieces then dried at 100 °C for 10 – 15 minutes in a vacuum oven. 5.56 ml of APTES was then added into a 50 ml deionized water-methanol solution (water: methanol volume ratio 3:1) while the solution was being magnetically stirred at a speed of 200 rpm. Next, 12 ml of acetic acid was added to the solution to restore the pH level to between 4.5 and 5. After all solutions had been added to the beaker, the stirring speed was increased to 400 rpm for 1 hour to fully hydrolyze the silane species. The surface silanisation was then achieved by soaking the sintered sample for 30 minutes at 40 °C . The silanised samples were subsequently washed through repeated rinsing with pure ethanol, then dried in air and stored in a desiccator.

Infiltrating the mold with PCL

High molecular weight polycaprolactone (PCL, Sigma Aldrich Product code 1003835078) was used as the infiltration material for this study due to its biocompatibility and mechanical toughness. First, an inverse 3D-printed polymer casting mold with the desired shape and depth was made using GreyPro V2 resin and Form 3+ printer from Formlabs (MA, US). The height and the length of the inverse cavity were the same as those of the nacre-like blocks. The 3D-printed parts were then used to create a silicone mold (PINKSIL, Barnes, AUS). The infiltration process took three steps: 1) filling the silicon mold with PCL beads first and subsequently melting them in a vacuum at 170 °C . 2) putting the sintered ceramic sample into the silicon mold and pressing it with a weight on top of it. 3) heating the sample at 170 °C for 1 hour with a weight on top of it to conclude the infiltration process. The samples and oven were then naturally cooled down at a rate of approximately 10 °C/min. After the infiltration, the surface of the composite was sanded to remove any polymer residue to make it ready for mechanical testing.

Mechanical testing

To evaluate the mechanical properties of the nacre-like composite, a four-point bending test was used to characterize the bending performance with an outer span of 50 mm and an inner span of 18 mm. The testing was maintained at a loading rate of 0.3 mm/min throughout the entire process. Force was obtained using a calibrated 2kN load cell. The displacement was captured using device crosshead displacements and corrected by manual image correlation using *in situ* imaging that was captured throughout testing. The bending stress and strain of all composites were computed under the assumption that the composite is homogeneous and linear elastic. The elastic modulus was measured as the initial slope of the stress-strain curve. The flexural strength was computed as the maximum flexural stress. The energy absorption was then derived from the area under the stress-strain curve. To compare the mechanical properties of nacre-like composite with the rule of mixture, the properties of its main constituents, alumina and PCL, were obtained via a three-point bending test and tensile test, respectively. The prediction value from the rule of mixture can then be calculated as a weighted sum of the mechanical properties of its main constituents based on their respective volume fractions in the composite. The details of the testing procedure and calculation process for the four-point bending, three-point bending, and tensile test are discussed in the Supplementary Information.

Data availability

All data needed to evaluate the conclusions in the paper are present in the paper and/or the Supplementary Information. All the additional data and the codes are available from the corresponding author upon request.

References

1 Mirkhalaf, M. Sustainable structural materials inspired by nature. *Journal of the American Ceramic Society*, e20710 (2025).

2 Eder, M., Amini, S. & Fratzl, P. Biological composites—complex structures for functional diversity. *Science* **362**, 543-547 (2018).
3 Wegst, U. G., Bai, H., Saiz, E., Tomsia, A. P. & Ritchie, R. O. Bioinspired structural materials. *Nature materials* (2014).
4 Meyers, M. A., Chen, P.-Y., Lin, A. Y.-M. & Seki, Y. Biological materials: structure and mechanical properties. *Progress in Materials Science* **53**, 1-206 (2008).
5 Barthelat, F., Tang, H., Zavattieri, P. D., Li, C. M. & Espinosa, H. D. On the mechanics of mother-of-pearl: a key feature in the material hierarchical structure. *Journal of the Mechanics and Physics of Solids* **55**, 306-337 (2007).
6 Yilmaz, E. D., Schneider, G. A. & Swain, M. V. Influence of structural hierarchy on the fracture behaviour of tooth enamel. *Philosophical transactions of the Royal Society A: Mathematical, physical and engineering sciences* **373**, 20140130 (2015).
7 Weaver, J. C. *et al.* The stomatopod dactyl club: a formidable damage-tolerant biological hammer. *Science* **336**, 1275-1280 (2012).
8 Ritchie, R. O. The conflicts between strength and toughness. *Nature Materials* **10**, 817-822, doi:10.1038/nmat3115 (2011).
9 Rabiei, R., Bekah, S. & Barthelat, F. Failure mode transition in nacre and bone-like materials. *Acta Biomaterialia* **6**, 4081-4089 (2010).
10 Liu, Q. *et al.* Nacre-inspired fabrication of robust and flexible photothermal protective films using a coordination-crosslinking self-assembly strategy. *Progress in Organic Coatings* **186**, 108014 (2024).
11 Vilchez, V., Zhou, S. & Bouville, F. Order induces toughness in anisotropic colloidal crystal composites. *Proceedings of the National Academy of Sciences* **122**, e2422532122 (2025).
12 Podsiadlo, P. *et al.* Ultrastrong and stiff layered polymer nanocomposites. *Science* **318**, 80-83 (2007).
13 Valashani, S. M. M., Barrett, C. J. & Barthelat, F. Self-assembly of microscopic tablets within polymeric thin films: a possible pathway towards new hybrid materials. *RSC Advances* **5**, 4780-4787 (2015).
14 Munch, E. *et al.* Tough, bio-inspired hybrid materials. *Science* **322**, 1516-1520 (2008).
15 Bouville, F. *et al.* Strong, tough and stiff bioinspired ceramics from brittle constituents. *Nature materials* **13**, 508-514 (2014).
16 Guo, R.-F., Hu, Z.-J., Shaga, A. & Shen, P. Development of a nacre-like metal-ceramic composite with a brick-and-mortar structure and high ceramic content. *Composites Part A: Applied Science and Manufacturing* **165**, 107347 (2023).
17 Li, D. *et al.* Nacre-inspired hierarchical framework enables tough and impact-monitoring epoxy nanocomposites. *Composites Part B: Engineering* **274**, 111246 (2024).
18 Li, D. *et al.* Toughing epoxy nanocomposites with Graphite-Nanocellulose layered framework. *Composites Part A: Applied Science and Manufacturing* **182**, 108159 (2024).
19 Le Ferrand, H., Bouville, F., Niebel, T. P. & Studart, A. R. Magnetically assisted slip casting of bioinspired heterogeneous composites. *Nature materials* **14**, 1172-1179 (2015).
20 Wang, H. *et al.* Tough and Conductive Nacre-inspired MXene/Epoxy Layered Bulk Nanocomposites. *Angewandte Chemie International Edition* **62**, e202216874 (2023).
21 Wang, Y. *et al.* Digital light processing-based additive manufacturing of orientation-controlled Al2O3 ceramics with improved damage tolerance. *International Journal of Applied Ceramic Technology* (2024).
22 Dimas, L. S., Bratzel, G. H., Eylon, I. & Buehler, M. J. Tough composites inspired by mineralized natural materials: computation, 3D printing, and testing. *Advanced Functional Materials* **23**, 4629-4638 (2013).
23 Hunter, G., Djumas, L., Brassart, L. & Molotnikov, A. Controlling failure regimes in Brick-and-Mortar structures. *Extreme Mechanics Letters* **51**, 101596 (2022).
24 Erb, R. M., Libanori, R., Rothfuchs, N. & Studart, A. R. Composites reinforced in three dimensions by using low magnetic fields. *Science* **335**, 199-204 (2012).
25 Vellayappan, M. V. *et al.* Fabrication of architectured biomaterials by multilayer co-extrusion and additive manufacturing. *Advanced Functional Materials* **33**, 2301547 (2023).

26 Amini, A., Khavari, A., Barthelat, F. & Ehrlicher, A. J. Centrifugation and index matching yield a strong and transparent bioinspired nacreous composite. *Science* **373**, 1229-1234 (2021).

27 Mirkhalaf, M. & Zreiqat, H. Fabrication and Mechanics of Bioinspired Materials with Dense Architectures: Current Status and Future Perspectives. *The Journal of The Minerals, Metals & Materials Society (JOM)*, 1-19 (2020).

28 Amini, A. *et al.* Nacreous Glass Composites with Superior Performance Engineered through Mechanical Vibration and Silanization. *Advanced Functional Materials*, 2405008 (2024).

29 Das, P. *et al.* Nacre-mimetics with synthetic nanoclays up to ultrahigh aspect ratios. *Nature communications* **6**, 5967 (2015).

30 Qi, P. *et al.* Quantifying the effects of geometric parameters on the elastic properties of multilayer graphene platelet films. *Advanced Materials*, 2502546 (2025).

31 Mirkhalaf, M., Dastjerdi, A. K. & Barthelat, F. Overcoming the brittleness of glass through bio-inspiration and micro-architecture. *Nature communications* **5**, 3166 (2014).

32 Yin, Z., Hannard, F. & Barthelat, F. Impact-resistant nacre-like transparent materials. *Science* **364**, 1260-1263 %@ 0036-8075 (2019).

33 Gupta, S., Esmaeeli, H. S. & Moini, R. Tough and Ductile Architected Nacre‐Like Cementitious Composites. *Advanced Functional Materials*, 2313516 (2024).

34 Roohani, I., Entezari, A. & Zreiqat, H. Liquid crystal display technique (LCD) for high resolution 3D printing of triply periodic minimal surface lattices bioceramics. *Additive Manufacturing* **74**, 103720 (2023).

35 Navarrete-Segado, P., Tourbin, M., Frances, C. & Grossin, D. Masked stereolithography of hydroxyapatite bioceramic scaffolds: From powder tailoring to evaluation of 3D printed parts properties. *Open Ceramics* **9**, 100235 (2022).

36 Barthelat, F. Growing a synthetic mollusk shell. *Science* **354**, 32-33 (2016).

37 Checa, A. G., Cartwright, J. H. & Willinger, M.-G. Mineral bridges in nacre. *Journal of structural biology* **176**, 330-339 (2011).

38 Ding, Z., Zreiqat, H. & Mirkhalaf, M. Rationally-designed self-shaped ceramics through heterogeneous green body compositions. *Materials Horizons* **9**, 2762-2772 (2022).

39 Mirkhalaf, M. *et al.* Personalized Baghdadite scaffolds: stereolithography, mechanics and in vivo testing. *Acta Biomaterialia* **132**, 217-226 (2021).

40 Griffith, M. L. & Halloran, J. W. Freeform fabrication of ceramics via stereolithography. *Journal of the American Ceramic Society* **79**, 2601-2608 (1996).

41 Tari, G., Ferreira, J., Fonseca, A. & Lyckfeldt, O. Influence of particle size distribution on colloidal processing of alumina. *Journal of the European ceramic society* **18**, 249-253 (1998).

42 Wu, H. *et al.* Effect of the particle size and the debinding process on the density of alumina ceramics fabricated by 3D printing based on stereolithography. *Ceramics International* **42**, 17290-17294 (2016).

43 Kelly, E. K. Flexure fatigue resistance of heat-curing and cold-curing polymethyl methacrylate. *J Am Dent Assoc* **74**, 1273-1276, doi:10.14219/jada.archive.1967.0435 (1967).

44 Chen, Z. *et al.* 3D printing of ceramics: A review. *Journal of the European Ceramic Society* **39**, 661-687 (2019).

45 Lee, J. H., Prud'homme, R. K. & Aksay, I. A. Cure depth in photopolymerization: Experiments and theory. *Journal of Materials Research* **16**, 3536-3544, doi:10.1557/JMR.2001.0485 (2001).

46 Oezkan, B., Sameni, F., Karmel, S., Engstrøm, D. S. & Sabet, E. A systematic study of vat-polymerization binders with potential use in the ceramic suspension 3D printing. *Additive Manufacturing* **47**, 102225 (2021).

47 McCurdy, K. & Laidler, K. Rates of polymerization of acrylates and methacrylates in emulsion systems. *Canadian Journal of Chemistry* **42**, 825-829 (1964).

48 Guzmán, E., Ortega, F. & Rubio, R. G. Forces controlling the assembly of particles at fluid interfaces. *Langmuir* **38**, 13313-13321 (2022).

49 Hinczewski, C., Corbel, S. & Chartier, T. Ceramic suspensions suitable for stereolithography. *Journal of the European Ceramic Society* **18**, 583-590 (1998).

50 Zhang, K. *et al.* High solid loading, low viscosity photosensitive Al2O3 slurry for stereolithography based additive manufacturing. *Ceramics International* **45**, 203-208 (2019).
51 Qian, C. *et al.* Effect of sintering aids on mechanical properties and microstructure of alumina ceramic via stereolithography. *Ceramics International* **49**, 17506-17523 (2023).
52 Tabrizian, P. *et al.* Bioactive and biocompatible nacre-like apatite-wollastonite/polymer composites with enhanced toughness and load-bearing capability. *Journal of the European Ceramic Society* **45**, 117397 (2025).
53 Li, Y.-L., Guo, R.-F., Hu, Z.-J. & Shen, P. Construction of nacre-mimetic composites with a "brick-and-mortar" architecture based on structural defects in ice-templating. *Materials & Design* **204**, 109668 (2021).
54 Sun, J. *et al.* 3D printing of layered ceramic/carbon fiber composite with improved toughness. *Additive Manufacturing* **50**, 102543 (2022).
55 Hunter, G., Djumas, L., Brassart, L. & Molotnikov, A. Effect of angled layers on failure regimes in brick-and-mortar structures. *Materials & Design* **218**, 110680 (2022).
56 Reilly, D. T. & Burstein, A. H. The mechanical properties of cortical bone. *JBJS* **56**, 1001-1022 (1974).
57 Liu, G. A step-by-step method of rule-of-mixture of fiber-and particle-reinforced composite materials. *Composite structures* **40**, 313-322 (1997).
58 Barinov, S. Work-of-fracture determination for brittle materials. *Journal of materials science letters* **12**, 674-676 (1993).
59 Rice, R. W., Freiman, S. W. & Becher, P. F. Grain-size dependence of fracture energy in ceramics: I, experiment. *Journal of the American ceramic society* **64**, 345-350 (1981).
60 Chen, W. *et al.* Effect of layer thickness on the enhanced strength and ductility of laminated Ti/Al composite. *Materials Science and Engineering: A* **859**, 144230 (2022).
61 Teng, X., Liu, H. & Huang, C. Effect of Al2O3 particle size on the mechanical properties of alumina-based ceramics. *Materials Science and Engineering: A* **452**, 545-551 (2007).

Acknowledgments

M Mirkhalaf acknowledges the Australian Research Council (ARC) Early Career Award (DE210100975). The team acknowledges key support from QUT, QUT CARF, and CARF Histology staff, particularly Mr. Nathaniel Raup, Dr Gregory Paterson, Dr Jun Zhang, Dr Yanan Xu, Ms. Liz Graham, Dr Jayanti Mendhi, and Ms. Felicity Lawrence. Z. Ding acknowledges support from QUT students: Myles Millar, Haoyu Wu, Joshua Borgeaud, Cobe Leclerc, Anna Tottoli, Alexander Rosario, Thomas Blacker, and Eden Brunner. The team acknowledges Amir Ghafari for useful discussions.

Author's contribution

Zizhen Ding: Conceptualization, Methodology, Validation, Formal Analysis, Visualization, Writing - Original Draft. **Reza Shakibanezhad**: Methodology, Writing - Review & Editing.

Travis Klein: Writing - Review & Editing, Supervision. **Mohammad Mirkhalaf**: Conceptualization, Methodology, Visualization, Resources, Writing - Original Draft, Review & Editing, Supervision, Funding acquisition.

Competing Interests

The authors declare no competing interests.

Supplementary Files

This is a list of supplementary files associated with this preprint. Click to download.

- SupplementaryinformationNC.docx